Inorganica Chimica Acta 487 (2019) 97–106

Contents lists available at ScienceDirect

Inorganica Chimica Acta

journal homepage: www.elsevier.com/locate/ica

Research paper

Synthesis, structural investigations and pharmacological properties of a new zinc complex with a N4-donor Schiff base incorporating 2-pyridyl ring

Mohammad Azam[a,*], Saikh Mohammad Wabaidur[a], Mohammad Jane Alam[b], Agata Trzesowska-Kruszynska[c], Rafal Kruszynski[c], Mahboob Alam[d], Saud I. Al-Resayes[a], Sourabh Dwivedi[e], Mohammad Rizwan Khan[a], Mohammad Shahidul Islam[a], Nader Talmas M. lbaqami[a]

[a] Department of Chemistry, College of Science, King Saud University, P.O. Box 2455, Riyadh 11451, Saudi Arabia
[b] Department of Physics, Aligarh Muslim University, Aligarh 202002, India
[c] Institute of General and Ecological Chemistry, Lodz University of Technology, Zeromskiego 116, 90-924 Lodz, Poland
[d] Division of Chemistry and Biotechnology, Dongguk University, 123 Dongdae-ro, Gyeongju 780-714, South Korea
[e] Department of Applied Physics, Aligarh Muslim University, Aligarh 202002, India

ARTICLE INFO

Keywords:
Zinc complex
Crystal structure
DFT studies
Molecular docking
Hirshfeld surface

ABSTRACT

A tetradentate Schiff base ligand, L (L = *N,N′*-bis(1-(2-pyridyl)ethylidene)-2,2-dimethylpropane-1,3-diamine) was used in the preparation of a new mononuclear Zn(II) complex, [Zn(L)Cl]. The complex was structurally investigated by elemental analyses, spectroscopic studies and single crystal X-ray crystallography. Furthermore, to obtain insights into the structure, the ground state geometry of zinc complex cation was examined by dispersion corrected DFT method i.e. B3LYP-D3 within unrestricted scheme. Intermolecular contacts in the crystal structure were calculated and quantified by examination of Hirshfeld surface and fingerprint plots. In addition, the pharmacological properties of the newly synthesized complex were examined to explore the *in vitro* antibiofilm activity against *P. aeruginosa*, and anticancer activity against Human breast adenocarcinoma (MCF-7) cell line. Furthermore, molecular docking study was also recorded to find out various modes of virtual interactions between the zinc complex cation and the active site of receptor (PDB: 1gzt).

1. Introduction

Zinc, the second most prominent trace element in human body, is associated with several biological and catalytic functions [1–7]. Over the past few years, several zinc complexes have been used extensively in treatment of various type of cancer, and considered as a promising alternative of *cis*-platin [8–11]. In addition, there are various reports in literature that zinc complexes possess potential luminescent properties [12], and play an important role in catalyst [13] optoelectronic light devices [13], enzyme inhibition [14], bio-imaging [15] and antibacterial agents [16]. The antibacterial property of zinc ion is significantly enhanced upon complexation with ligand, particularly with nitrogen containing ligands [17]. Among various nitrogen containing ligands [18], pyridyl ligands have received considerable attention in coordination chemistry due to their strong chelating property and construction of distinct coordination architectures [19]. Herein we are focused on the preparation of a Zn(II) complex, [Zn(L)Cl], derived from L. The ligand, L is prepared as described in the literature [20–22]. To get insights into the structure, the computational study of zinc complex cation is carried out, and found to be close with experimental results. In addition, Hirshfeld surface analysis is also described to study the adjacent intermolecular interactions in the present study. The pharmacological behaviour of newly synthesized zinc complex is investigated to explore the anticancer activity against MCF-7 cell line, and *in vitro* antibiofilm activity against *P. aeruginosa.* The molecular docking study [23] is also recorded to assess the binding potential and the mode of interactions of zinc complex with the sequence of amino acids of protein of *P. aeruginosa.* In addition, the proper orientation of the complex buried inside of the diseases carrying active sites of a highly pathogenic, contagious and drug resistant bacteria protein is also verified by *in silico* approach.

* Corresponding author.
E-mail address: azam_res@yahoo.com (M. Azam).

https://doi.org/10.1016/j.ica.2018.12.009
Received 26 October 2018; Received in revised form 12 November 2018; Accepted 4 December 2018
Available online 05 December 2018
0020-1693/

2. Experimental

2.1. Materials and physical measurements

All chemicals and reagents used in this article were obtained from Sigma-Aldrich, and used as received. FT-IR spectra were recorded using KBr pallet on Perkin Elmer 621 infrared spectrophotometer. ^{1}H and ^{13}C NMR spectra were carried out on JEOL-400 spectrometer in d_6-DMSO. Elemental analysis was performed on Elementar Varrio EL analyzer. ESI-MS and electronic spectra were carried out on Micromass Quattro Premier Tandem MS spectrometer and Pharmacia LKB-Biochem spectrophotometer, respectively. Fluorescence spectra were obtained in acetonitrile using RF6000 Spectro Fluorophotometer.

2.2. Synthesis of [Zn(L)Cl]

The ligand, L (85 mg, 0.28 mmol) was dissolved in 20 ml ethanol followed by the addition of $ZnCl_2{\cdot}2H_2O$ (38 mg) in 1:1 molar ratio. The resultant solution was magnetically stirred for 5 h at room temperature. Slight turbidity appeared which was separated out. The clear solution was dried under vacuum followed by washing with ditheylether and hexane. The orange colored crystals were obtained upon re-crystallization in ethanol.

Yield 55%, color orange, mp 145 °C; Molecular Formula $C_{42}H_{62}Cl_6N_8O_3Zn_3$; Anal. Calc.: C, 44.41; H, 5.50; N, 9.87 Found: C, 44.33; H, 5.48; N, 9.79%. ESI-MS (*m/z*), 1136.8 $(M+H)^+$, ^{1}H NMR (DMSO-d_6): (ppm): 7.34–8.71 (m, Py-H), 3.58 (s, –C**H**$_2$), 2.42 (s, C**H**$_3$–C═), 1.12 (s, (C**H**$_3$)$_2$C–); ^{13}C NMR ($CDCl_3$): (ppm) 165.3 (–**C**═N), 152.9–120.1 (Py-**C**), 67.1 (–**C**H$_2$–N), 25.6 (**C**H$_3$-C═N), 55.8 ((CH$_3$)$_2$–**C**–(CH$_2$)$_2$),13.5 (–**C**H$_3$); IR (KBr cm^{-1}): 1600 $\upsilon_{(CH=N)}$.

2.3. Crystal structure study

The crystallographic data for zinc complex was collected on Rigaku Synergy Dualflex automatic diffractometer accompanied by Pilatus 300 K detector, and equipped with mirror monochromated MoK_α (λ = 0.71073 Å) radiation at 100.0(1) K. The whole crystallographic and refinement details are provided in Table 1. The structure was solved by partial structure expansion method, and all the non-hydrogen atoms in the structure were subjected to anisotropic refinement by full-matrix, least-squares technique on F^2. All calculations were performed by SHELXS [24], SHELXL [24] and SHELXTL [25] software. Atomic scattering factors were taken from International Tables for Crystallography [26]. Selected bond lengths are given in Table 2 and intermolecular interactions in Tables 3 and 4, respectively.

Table 1
Crystal and structure refinement data of compound **1**.

Compound	**1**
Empirical formula	$C_{42}H_{62}Cl_6N_8O_3Zn_3$
Formula weight	1135.80
Crystal system, space group	Monoclinic, $P2_1/c$ (No. 14)
Unit cell dimensions [Å, °]	a = 12.1287(4)
	b = 17.3199(5)
	c = 23.6610(7)
	β = 90.084(3)
Volume [Å^3]	4970.4(3)
Z, Calculated density [Mg/m^3]	4, 1.518
F(0 0 0)	2344
Crystal size [mm]	0.098, 0.093, 0.076
θ range for data collection [°]	3.494 to 25.049
Index ranges	$-14 \le h \le 14$, $-20 \le k \le 20$,
	$-28 \le l \le 28$
Reflections collected/unique	83,644/8784 [$R_{(int)}$ = 0.0861]
Completeness [%]	99.7 (to θ = 25°)
Data/restraints/parameters	8784/0/569
Goodness-of-fit on F^2	1.075
Final R indices [$I > 2\sigma(I)$]	$R1$ = 0.0424, w$R2$ = 0.1137
R indices (all data)	$R1$ = 0.0540, w$R2$ = 0.1215
Largest diff. peak and hole [e·Å^{-3}]	1.169, −1.102

2.4. Computational details

All calculations were performed using unrestricted scheme at UB3LYP-D3/6-31G(d,p) level of theory implemented in Gaussian-WebMO interface [27]. The dispersion corrected functional B3LYP-D3, where Grimme's D3 correction [28] is used for long range dispersion interactions, particularly for the compounds having inter or intramolecular interactions. In this work, the molecular geometry of the ground state of zinc complex cation was fully optimized at same level of theory where the input geometry was taken from the crystallographic coordinates. Vibrational frequencies calculation was also carried out in the harmonic approximation at optimized geometry. All FT-IR vibrations shown are actual, and display the geometry to the minima on potential energy surface. The deviations from the experimental findings are due to the exclusion of an harmonicity and various other approximations used in theory for vibrational frequency calculations. Furthermore, these frequencies were scaled down using uniform scaling factor, 0.967 to match with the experimental results [29]. Some important vibrational bands were also assigned with great accuracy by animated modes using GaussView 5 program [30]. The Lorentzian band shape with FWHM at 8 cm^{-1} was employed to plot simulated calculated IR spectrum. The parameters provided in this work viz. dipole moment, HOMO/LUMO energies, gap and molecular electrostatic potential (MEP) surface were obtained at same level of theory. Natural bond orbital (NBO) analysis is also performed to study some important interactions within the complex cation. The stabilization energy $E^{(2)}$ associated with delocalization (2e-stabilization) is estimated between donor NBO (bonding) and acceptor NBO (antibonding). The resulting molecular geometry, HOMO-LUMO and MEP plots were visualized using GaussView 5 program [30]. The experimental bond lengths and angles were found to be quite close with the calculated data obtained at UB3LYP-D3/6-311G(d,p) level of theory [Table 2]. Hirshfeld surfaces calculations were made using CrystalExplorer17 [31] program. Solvent molecules were removed from the CIF file, and then applied to the CrystalExplorer program17 for calculations. All hydrogen bond lengths were automatically revised to standard neutron values (CH = 1.083 Å). The decomposed 2D fingerprint plots were made using the surface property (−0.21 to 2.6 Å) with the *de* and *di* distance scales shown on the axes of the graph.

2.5. Antibiofilm activity

The antibiofilm activity of the complex was examined by the previously established methods [32]. *P. aeruginosa* used for this assay was grown in luria broth along with increasing concentration of complex (0–50 μg/ml) into 6 well plates at 37 °C for 96 h. Each well was stained with crystal violet (0.1%) and solubilized with 95% ethanol. The quantification of antibiofilm activity was determined by optical density at 570 nm.

2.6. Cell culture and exposure

MCF-7 cell lines were cultured in DMEM/F-12 medium supplemented with 10% FBS and 100 U/mL penicillin–streptomycin at 5% CO_2 and 37 °C to examine the cell viability of zinc complex estimated through MTT assay [33] followed by sonication for 10 min at 40 W.

2.7. Molecular docking study

Molecular docking was carried out using various software such as Discovery Studio V4.0, (Accelry Inc., CA, USA), Autodock tools [34], Molegro Virtual Docker [35,36], including Patchdock [37,38] and EMBL-EBI servers [39] to get the trustworthy results in the procedure.

Table 2
Selected structural data of zinc complex [Å, °].

DFT[a]						
Zn1–N1	2.139(3)	2.096	Zn21–N21	2.166(3)	Zn41–Cl41	2.2648(10)
Zn1–N2	2.115(3)	2.061	Zn21–N22	2.083(3)	Zn41–Cl42	2.2742(11)
Zn1–N3	2.112(3)	2.162	Zn21–N23	2.139(3)	Zn41–Cl43	2.2570(10)
Zn1–N4	2.131(3)	2.128	Zn21–N24	2.100(3)	Zn41–Cl44	2.2881(11)
Zn1–Cl1	2.2701(9)	2.304	Zn21–Cl21	2.2674(9)		
C6–N2	1.282(4)	1.323	C26–N22	1.290(4)		
N2–C8	1.476(4)	1.453	N22–C28	1.472(4)		
C12–N3	1.472(4)	1.458	C32–N23	1.473(4)		
N3–C13	1.288(4)	1.295	N23–C33	1.277(5)		
N1–Zn1–N2	77.39(11)	78.51	N21–Zn21–N22	77.34(11)	Cl41–Zn41–Cl42	107.68(4)
N1–Zn1–N3	135.81(11)	122.25	N21–Zn21–N23	156.38(11)	Cl41–Zn41–Cl43	113.81(4)
N1–Zn1–N4	98.51(11)	97.42	N21–Zn21–N24	98.58(11)	Cl41–Zn41–Cl44	107.61(4)
N2–Zn1–N3	87.29(11)	85.16	N22–Zn21–N23	87.68(11)	Cl42–Zn41–Cl43	107.40(4)
N2–Zn1–N4	153.45(11)	156.12	N22–Zn21–N24	131.51(11)	Cl42–Zn41–Cl44	113.45(4)
N3–Zn1–N4	77.47(10)	76.66	N23–Zn21–N24	77.70(11)	Cl43–Zn41–Cl44	107.04(4)
N3–Zn1–Cl1	121.88(8)	137.14	N22–Zn21–Cl21	124.18(8)		
N2–Zn1–Cl1	109.46(8)	103.18	N24–Zn21–Cl21	104.30(8)		
N4–Zn1–Cl1	97.06(8)	100.49	N23–Zn21–Cl21	107.90(8)		
N1–Zn1–Cl1	102.30(8)	100.63	N21–Zn21–Cl21	95.65(8)		

[a] Optimized structural parameters for Zn complex cation.

Table 3
Hydrogen bonds geometry of zinc complex [Å, °].

D–H···A	d(D–H)	d(H···A)	d(D···A)	< (DHA)
O41–H41O···Cl44	0.82	2.54	3.354(3)	172.5
O43–H43O···Cl42^{i}	0.81	2.58	3.373(4)	165.5
O44–H44O···O41	0.83	1.99	2.808(7)	169.2
O44–H44P···O43	0.86	1.89	2.736(7)	167.3
C2–H2···Cl42^{i}	0.93	2.93	3.617(4)	132.3
C2–H2···Cl43^{i}	0.93	2.89	3.692(4)	144.9
C8–H8A···Cl43^{ii}	0.97	2.65	3.608(4)	167.4
C10–H10A···Cl1	0.96	2.72	3.679(4)	172.3
C12–H12A···Cl41^{iii}	0.97	2.82	3.746(4)	160.3
C12–H12B···O44^{iv}	0.97	2.52	3.340(6)	142.5
C14–H14A···Cl41^{iii}	0.96	2.80	3.674(4)	151.1
C14–H14C···O41^{iv}	0.96	2.57	3.486(5)	159.9
C19–H19···O43	0.93	2.54	3.249(5)	132.8
C27–H27A···O44	0.96	2.53	3.320(7)	139.8
C27–H27C···Cl43	0.96	2.84	3.774(4)	163.9
C28–H28A···O44	0.97	2.26	3.219(6)	170.9
C30–H30C···Cl44	0.96	2.74	3.699(4)	174.9
C31–H31A···Cl21	0.96	2.76	3.721(4)	176.8
C32–H32A···Cl42	0.97	2.97	3.745(4)	137.3
C32–H32B···Cl41^{v}	0.97	2.71	3.650(4)	162.5
C37–H37···Cl21^{vi}	0.93	2.78	3.505(4)	135.6
C38–H38···Cl41^{iv}	0.93	2.78	3.609(4)	148.4
C39–H39···Cl44^{iv}	0.93	2.83	3.513(4)	130.7
C41–H41B···Cl43	0.97	2.82	3.615(4)	139.8
C43–H43B···Cl41^{i}	0.97	2.88	3.565(6)	128.8

Symmetry transformations used to generate equivalent atoms: (i) x + 1, y, z; (ii) −x + 1, −y + 1, −z + 1; (iii) x + 1, −y + 3/2, z − 1/2; (iv) x, −y + 3/2, z − 1/2; (v) −x, y + 1/2, −z + 3/2; (vi) −x, −y + 2, −z + 1.

X-Ray diffraction structural data of protein (1gzt.pdb) named *Pseudomonas aeruginosa* [40] with resolution 1.3 Å was taken from the Protein Data Bank followed by the detachment of water and solvent molecules of the complex from the PDB file. The lost assignments such as proper bonds, bond orders, hybridization and charges were assigned, and the receptor conformation was suppressed using the Molegro Virtual Docker protein preparation wizard. The AutoDock tool (ADT) graphical interface was used to repair the PDB file: polar hydrogen was added, Kollman charges were computed and nonpolar hydrogen atoms were merged with the carbon atoms for the proper execution of molecular docking. In the preparation of the ligand for molecular docking, the solvent and the anionic part; $ZnCl_4$ of the X-ray structure of the metal complex were removed and saved in MOL format using the MERCURY program. The three-dimensional structures of the zinc complex cation was geometrically optimized using the B3LYP/6-311 g(d,p) level under Gaussian 09 and the structure saved in PDB format for further implementation. The X-ray structure of metal complex was saved in PDB format using the MERCURY program. The partial charge of PDB file was further checked by the ADT software (version 1.5.6) to assign the charge of non-polar hydrogen to the atom to which the hydrogen was connected and saved in same format. The amino acids present at the active site of the receptor were identified by FTSite server [41] and applied in PatchDock under advanced process. The PatchDock server program furnished ten top possible docked models for the most probable structure sorted on the basis of the energetic parameters; geometric shape complementarity score. PatchDock outcomes were further polished by FireDock [42,43]. The result of the most favorable binding score of docked pose was selected as the resultant complex structure. The binding mode and associated interactions of the top docking result among ten models were explored and visualized using the Discovery studio software [44].

Table 4
Stacking interactions in compound **1** [Å, °]. Cg(1), Cg(2), Cg(3) indicates the centroids of six-membered pyridine rings (R) containing N1, N4, N21 and N24 atoms respectively, α is a dihedral angle between planes I and J, β is an angle between Cg(I)-Cg(J) vector and normal to plane I and d_p is a perpendicular distance of Cg(I) on ring J plane.

R(I)···R(J)	Cg···Cg	α	β	d_p
Cg(1) ···Cg(1)^{i}	4.296(2)	0.00	33.2	3.5951(14)
Cg(1)···Cg(4)^{ii}	4.5596(19)	4.46(16)	38.3	3.6362(14)
Cg(2)···Cg(3)	3.857(2)	1.49(16)	18.1	3.6940(13)
Cg(3)···Cg(2)	3.857(2)	1.49(16)	16.7	3.6650(14)
Cg(4)···Cg(1)^{iii}	4.5597(19)	4.46(16)	37.1	3.5791(14)
Cg(4)···Cg(4)^{iv}	4.1300(19)	0.00	28.7	3.6224(14)

Symmetry transformations used to generate rings: (i) −x + 2, −y + 1, −z + 1; (ii) x + 1, y, z; (iii) x − 1, y, z; (iv) −x, −y + 2, −z + 1.

3. Results and discussion

3.1. Molecular geometry

All atoms of studied zinc complex occupy general positions, and a perspective view of asymmetric unit is shown in Fig. 1. There are two complex cations and one complex anion in asymmetric unit of the complex. Additionally, one water and two ethanol molecules are placed outside the coordination sphere. The two coordination moieties i.e. the

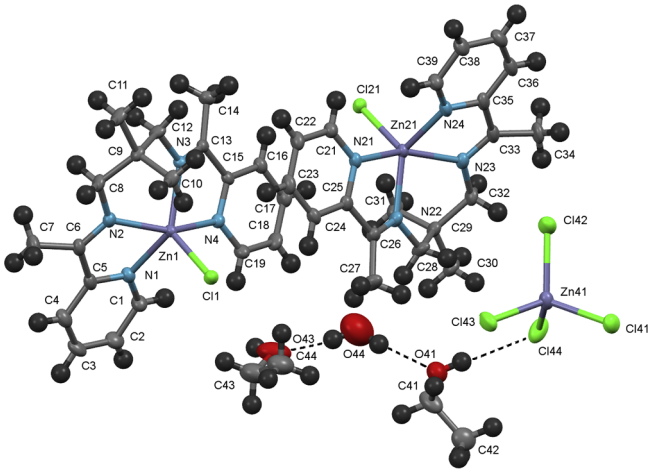

Fig. 1. The molecular structure of zinc complex at 50% probability of displacement ellipsoids. The hydrogen atoms are drawn as a spheres of arbitrary radius of 0.3 Å. The hydrogen bonds existing between species located in the asymmetric unit are represented by dashed lines.

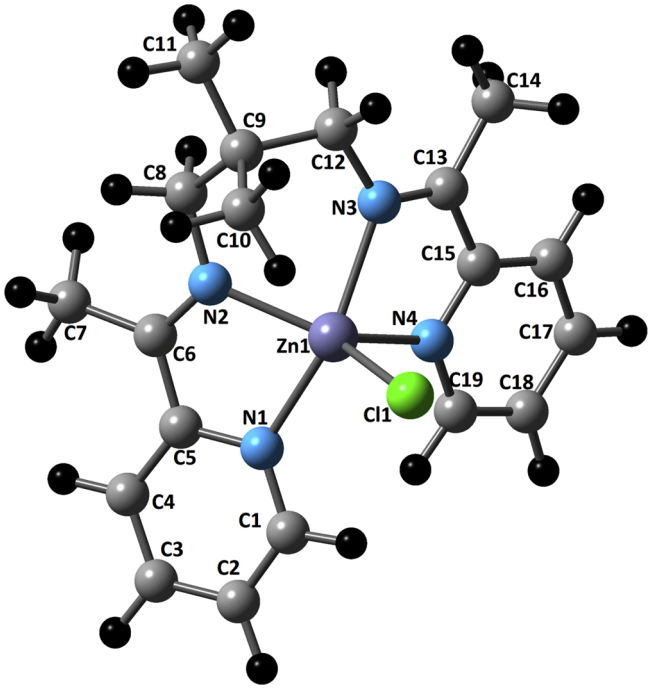

Fig. 2. Optimized geometry of the zinc complex cation.

zinc complex cation in asymmetric unit are same. Therefore, for the sake of simplicity only one moiety (zinc complex cation) is considered in theoretical calculations [Fig. 2]. The optimized molecular geometry of the ground state of zinc complex cation alone has been obtained at same level of theory [Fig. 2]. The dipole moment for the optimized geometry is found to be 8.4 Debye for the Zn complex cation. The coordination moieties with L consist of pseudosymmetry mirror plane going through central atoms, chloride anions and methyl groups of 2,2-dimethylpropane moiety. The $[ZnCl_4]^-$ ion have four threefold rotation axes going along the Zn–Cl bond. Both the coordination moieties with L possess similar conformation, and the root mean squares deviation of superimposed moieties is 0.129(6) Å (the most distant C12 and C28 atoms are separated at 0.226(4) Å). The zinc ions are five (Zn1 and Zn21) and four (Zn41) coordinated. In first case, zinc ion is coordinated by two imine nitrogen atoms [(Zn1–N2 and Zn1–N3) and (Zn21–N22 and Zn21–N23)], two pyridyl nitrogen atoms [(Zn1–N1 and Zn1–N4) and (Zn21–N21 and Zn21–N24)] and one chloride ion (Zn1–Cl1) and (Zn21–Cl21). In second case, zinc ion is coordinated by four chloride anions. The Zn–N_{imine} bond distances, Zn1–N3 2.112(3) Å, Zn1–N2 2.115(3) Å, Zn21–N22 2.083(3) Å, Zn21–N23 2.139(3) Å and Zn–N_{py} distances, Zn1–N1 2.139(3) Å, Zn1–N4 2.131(3) Å, Zn21–N21 2.166(3) Å, Zn21–N24 2.100(3) Å, are typical for such type of complexes [20,21]. The Zn–Cl distances are Zn1–Cl1 2.2701(9), Zn21–Cl21 2.2674(9) Å.

According to the method of Kepert [45], the coordination environment of Zn1 and Zn21 metal atoms can be described as strongly distorted trigonal bipyramid with the N2/N4, N21/N23 nitrogen atoms located at the polyhedron apexes, and of Zn41 atom as tetrahedron. The calculated Addison and Yang geometry indices [46,47] suggest that the coordination polyhedron around Zn1 atom adopts distorted square pyramidal geometry (τ_5 is about 0.3), around Zn21 atom adopts mixed square pyramidal-trigonal bipyramidal geometry (τ_5 is about 0.4), and around Zn41 atom adopts slightly distorted tetrahedral geometry (τ_4 and τ_4' are about 0.9). Nevertheless of the method (i.e. nevertheless of differences originating from different approaches described by Kepert, Addison and Yang) it can be stated that Zn1 and Zn21 atoms coordination polyhedra are considerably distorted and observed geometry is transitional between square pyramidal (with the apex located at chlorine atom) and trigonal bipyramidal one [Supplementary information Fig. S1 and Table S1 for comparison of unit A (Zn1) with unit B (Zn21) of Zn-complex cation and bond angles].

The presented compound, Bis{Chloro((*N*,*N*′-bis(1-(2-pyridyl)ethylidene)-2,2-dimethylpropane-1,3-diamine)zinc(II)] [tetrachloratezincate (II)] is the first example of L as a building block for construction of crystal net containing the $[MX_4]^{2-}$ coordination moiety (where M = any metal cation, X = any halogen anion), as well as for formation of a zinc coordination complex with confirmed structure. Using the above ligand, several complexes incorporating cobalt, iron, nickel and copper have been mentioned in literature [20,21,48–50]. The weighed least squares planes calculated thorough the pyridine moieties are inclined at 31.31(8) and 35.35(8)° within each complex cation, and these values are found in the range of existing compounds mentioned in literature [20,21,48–50]. The C—N bond lengths analysis suggests that the double bonds are fully localized within methanimine moieties [Table 2]. The Zn–N bond lengths (Table 2) are typical for zinc coordination compounds [3,51–55] and differ no more than 0.08 Å from the mean bond length (2.09(7) Å for 63,763 values observed in 20,574 compounds [56]). Similarly, the observed Zn–Cl bond lengths (Table 2) oscillate up to 0.03 Å from the men value of 2.26(6) Å (calculated for 9101 values founded in 3514 compounds [56]) and such variations are typical for zinc coordination compounds [57]. The XRD data is found in good agreement with optimized structural parameters and the discrepancy arises due to the fact that the crystal lattice distortion exists in real molecules [58]. The large deviations are noticed only for the bond angles Cl41–Zn41–Cl42 and Cl43–Zn41–Cl44 [Table 2]. This results from the fact that the optimized geometry does not have same interactions as presented in crystal for the moiety of zinc cation coordinated by four chloride anions.

The solvent molecules and complex anions are linked *via* O—H···O and O—H···Cl intermolecular hydrogen bonds [Table 3] to the hydrogen bonded chain extending along crystallographic [1 0 0] axis. These bonds form $C_4^4(10)$ quaternary graph set of lowest degree (up to tertiary graph set all motifs are the finite ones) [59]. The complex cations do not form the classical hydrogen bonds, as a consequence of lack of classical hydrogen bond donors within them and saturation of the ethanol molecules hydrogen bond donors by complex anions. The multiple weak C—H···O and C—H···Cl intermolecular hydrogen bonds [60] [Table 3] expand above described chains and complex cations to the three-dimensional supramolecular net. Each complex cation is linked through C—H···Cl intermolecular hydrogen bonds to the three neighbouring complex anions and through C—H···O intermolecular hydrogen bond to one water molecule. The complex cation containing

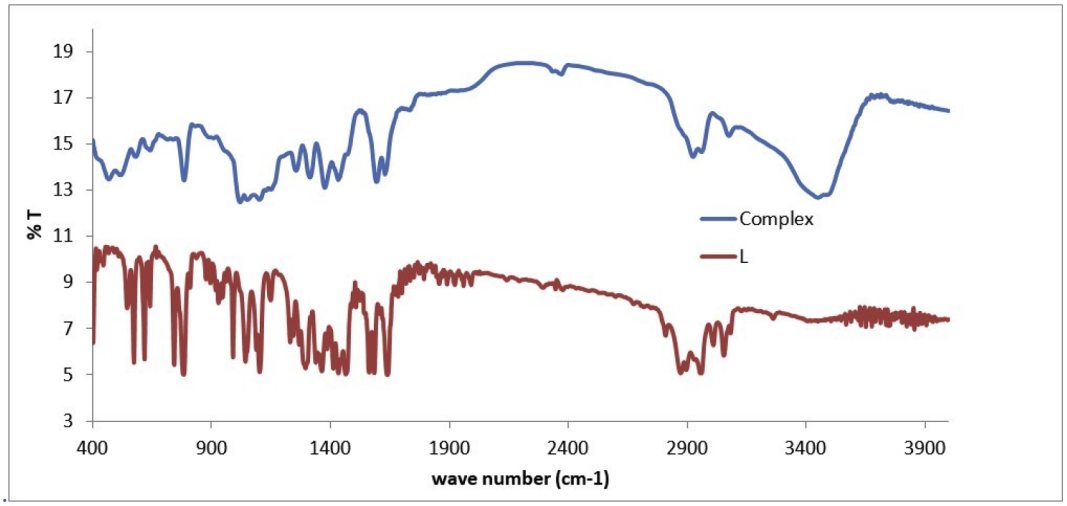

Fig. 3. Comparison of IR spectra of L, and its zinc complex with shifted baseline.

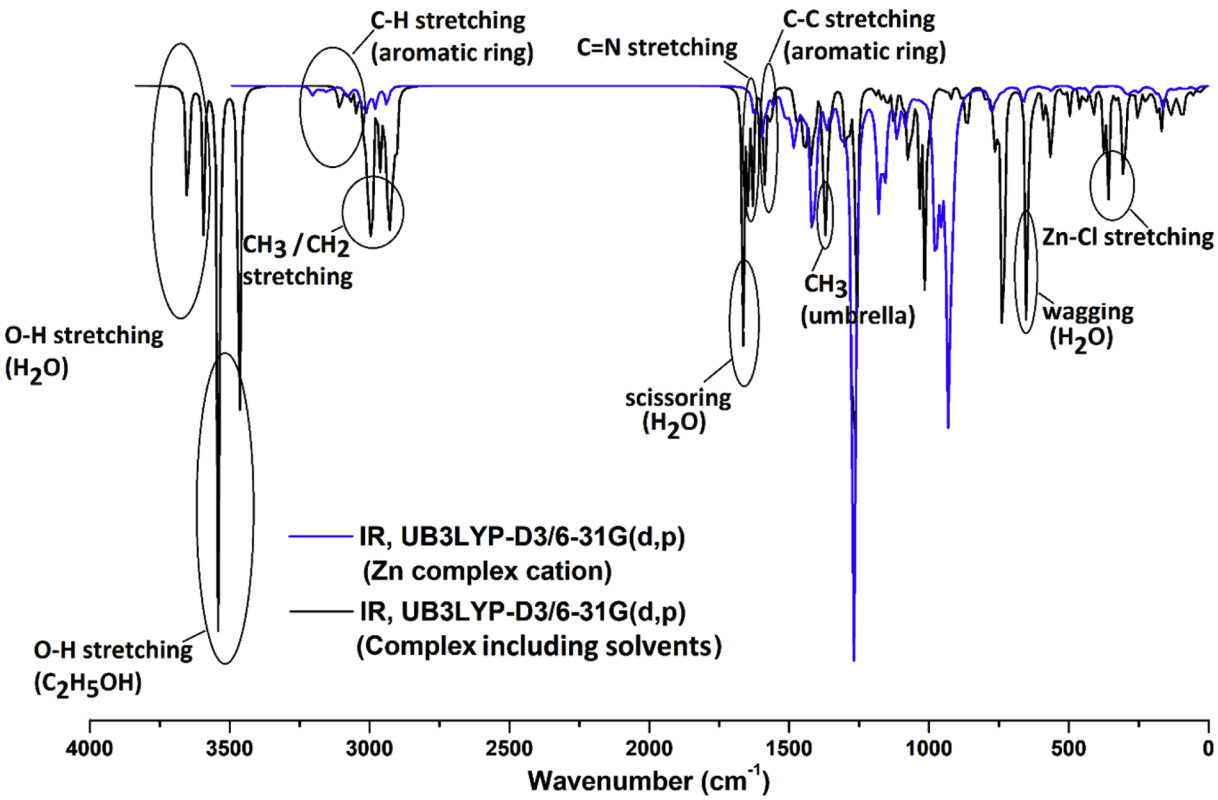

Fig. 4. Simulated IR spectra of Zinc-complex cation (blue colour) and Zn-complex including solvents (black colour). (For interpretation of the references to colour in this figure legend, the reader is referred to the web version of this article.)

Zn1 atom additionally forms C—H···O intermolecular bonds to the two ethanol molecules of outer coordination sphere. Each ethanol molecule acts a donor of C—H···O intermolecular bond toward one complex anion. Due to absence of any hydrogen bonds donors, the complex anion acts solely as hydrogen bonds acceptor. The intramolecular π···π staking interactions [61] assemble the complex cations of supramolecular net to the π···π bonded layer extending along crystallographic (0 0 1) plane (each complex cations interacts with three neighbouring in the crystal net cations).

3.2. IR spectral analysis

The characteristic peak due to $\upsilon_{(C=N)}$ vibration at 1640 cm^{-1} in the IR spectra of L is shifted and appears at 1600 cm^{-1} in the spectra of the complex [Fig. 3] [62,63].

Simulated IR spectra along with some important vibrational assignments for the complex cation with and without $ZnCl_4$/solvents are shown in Fig. 4. The vibrational bands in the experimental IR spectrum are found to match well with theoretical one. Multiple non-covalent interactions within this complex significantly affect the IR spectra. A broad band at 3450 cm^{-1} shows the presence of O—H group (hydrogen bonded) in solvents. The C—H stretching vibrations in aromatic ring form bands at higher wavenumber than those observed for oscillators of $–CH_2/CH_3$ groups. A band at 3074 cm^{-1} is assigned to C—H stretching vibrations in aromatic ring, whereas vibrations at 2961 cm^{-1} and 2921 cm^{-1} are assigned to C—H stretching of $–CH_2/CH_3$ groups. The

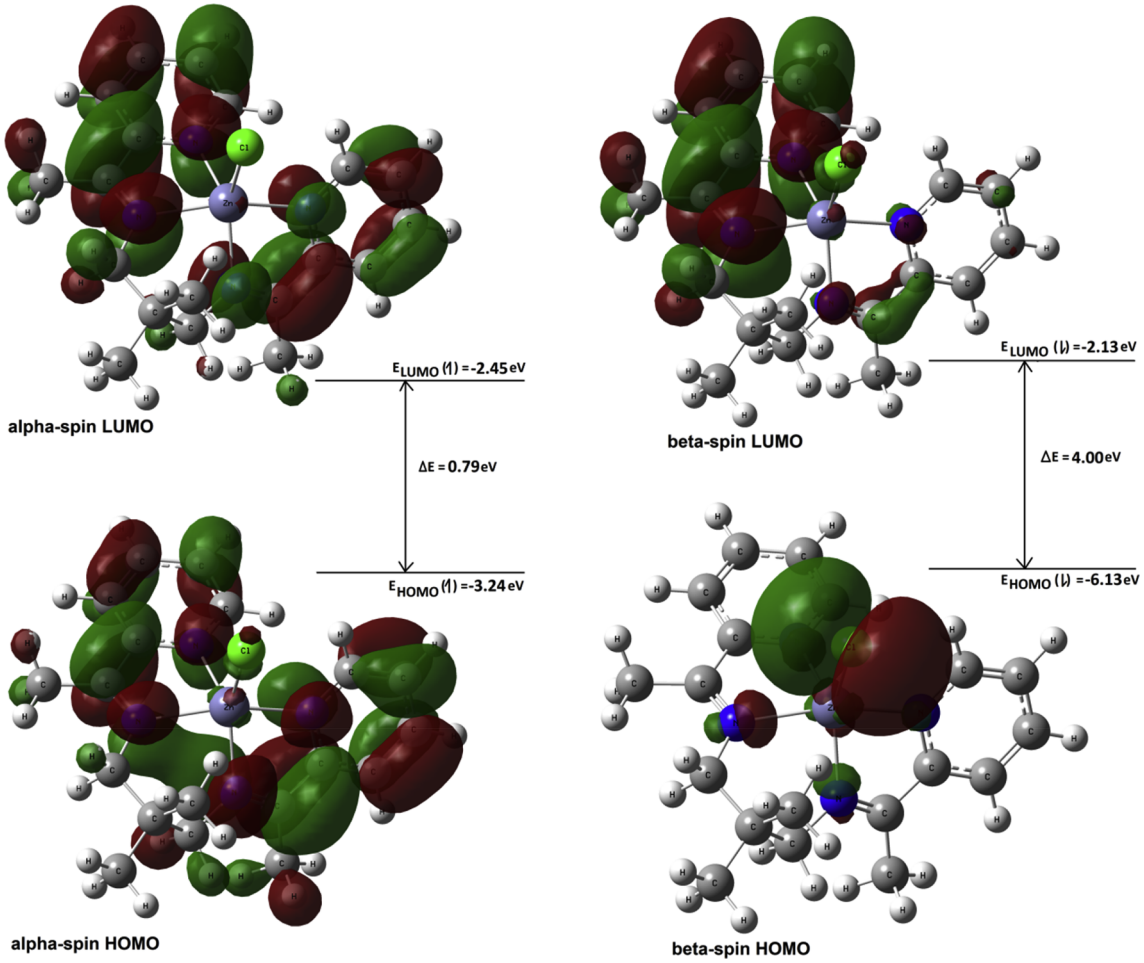

Fig. 5. HOMO and LUMO orbitals of Zn complex cation.

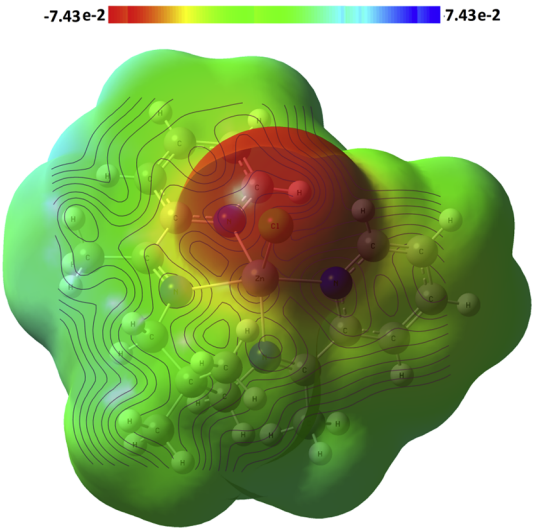

Fig. 6. MEP surface of the Zn complex cation.

C═N and C═C stretching vibrations are estimated respectively at higher and lower wavenumber around 1600 cm^{-1}. The Zn–Cl stretching vibrations are monitored below 400 cm^{-1}. The bands appeared in the experimental IR spectra are found in closed agreement with the theoretical one. Thus, the simulated along with experimental IR spectra confirm the Zn complex cation structure.

3.3. Frontier molecular orbitals, molecular electrostatic potential map and NBO analysis

The molecular geometry chosen for the present calculations have doublet multiplicity. Therefore, frontier molecular orbitals (highest occupied molecular orbitals (HOMO) and lowest unoccupied molecular orbitals (LUMO)) are split into alpha (spin ↑) and beta (spin ↓) molecular orbitals. The isodensity plots along with energy values of frontier molecular orbitals are shown in Fig. 5. The electronic properties depend mostly on frontier molecular orbitals and band gap of the molecule. The energy values of these orbitals define quantitatively the chemical reactivity like chemical potential, electrophilicity, chemical hardness, softness etc. The energy gaps for alpha and beta spin molecular orbitals are estimated and shown in Fig. 5. The low HOMO and LUMO gap defines the high chemical reactivity and low kinetic stability of the compound. The HOMO and LUMO are localized over the complex except some atoms for alpha (spin ↑) whereas the HOMO is spread over Zn, Cl and N atoms, and LUMO is mainly on aromatic ring for beta (spin ↓) [Fig. 5].

Spatial diagrams of HOMO and LUMO [Fig. 5] show the charge delocalization upon excitation. The molecular electrostatic potential (MEP) map of present complex is computed to investigate its binding properties. The MEP surface and contour plot with colour ranging deepest red to deepest blue are shown in Fig. 6. The most of the regions of present molecule are neutral as shown by green color. The negative electrostatic potential (red color) is located over the chlorine atom [Fig. 6]. The regions of high and low electrostatic potential are described by dominancy and deficiency of electrons, respectively. The

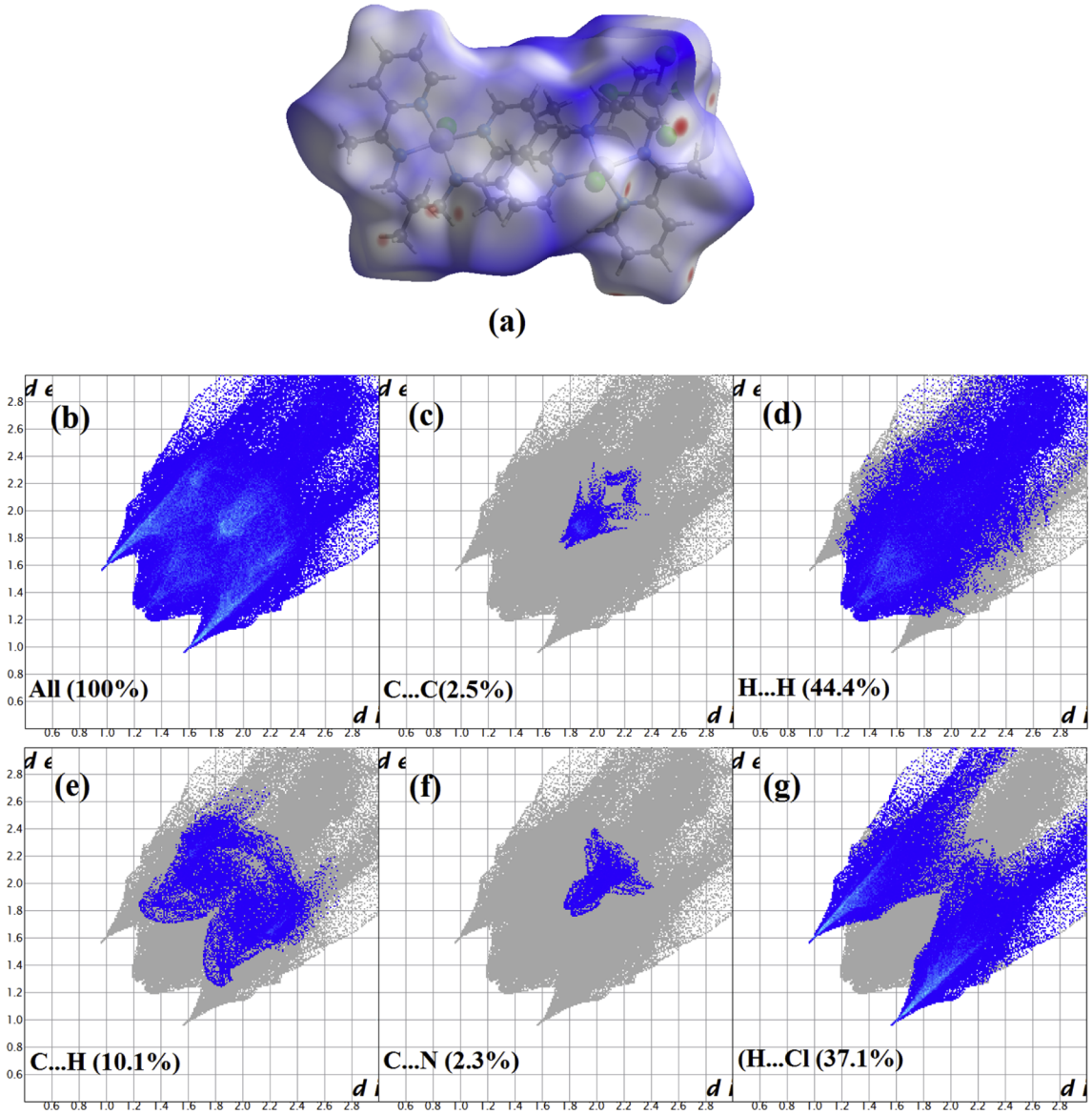

Fig. 7. (a) Hirshfeld surface mapped over d_{norm} (b) 2D fingerprint plot linked with close contact interaction with all atoms, (b) percentage contributions of close contact interactions of C···C (c), H···H (d), C···H (e), C···N (f) and H···Cl (g) in Zn-complex.

positive and negative potential of the MEP for present complex is likely the most preferred site for the nucleophilic and electrophilic attack, respectively.

Some important interactions within complex have been examined using stabilization energy, $E^{(2)}$, by NBO analysis. The larger value of $E^{(2)}$ reveals the more intensive electron donor–acceptor interaction. Some important $E^{(2)}$ values are reported as 17.03, 18.01, 19.81, 15.23, 42.07 kcal/mol for donor-acceptor NBO interactions N49···Zn1, N34···Zn1, N18···Zn1, N3···Zn1 and Cl2···Zn1 respectively.

3.4. Hirshfeld surface analysis

Hirshfeld surface and the associated 2D fingerprint plots were employed to specify the various intermolecular contacts involved in complex by the CrystalExplorer17 [31]. The Hirschfeld surface of the complex was shown in the Fig. 7a indicating the area mapped over a d_{norm} range from −0.21 to 2.6 Å. The surface is transparently displayed to allow visualization of the complex moiety in a similar orientation. Large circular depressions (sharp red), blue areas and white area which appear on the surfaces indicate the short contacts (hydrogen bonding), longer contacts and contacts with distances equal to the sum of the van der Waals radii, respectively [Fig. 7]. In addition, the 2D fingerprint plots clarified the individual close contacts of the pairs of atoms and the contributions of the different contacts [Fig. 7b–g]. The two-dimensional fingerprint plots with a large bump represent the H···H contacts (Fig. 7d) and the intense spikes indicate strong H···Cl interactions (Fig. 7g), while the wing expansion displays the interaction C···H (Fig. 7e) in molecule. The major contribution to crystal packing comes from H···H interactions (44.4%, Fig. 7d) followed by H···Cl interactions that contribute 37.1% compared to the other contacts present in the crystalline structure of the complex. Other weak interactions present in the complex were C—C (2.5%, Fig. 7c), C—N (2.3%, Fig. 7f) and C–Cl (0.3%, not shown in Fig. 7). An analysis of such illustrations for intermolecular contacts is acceptable with those observed by

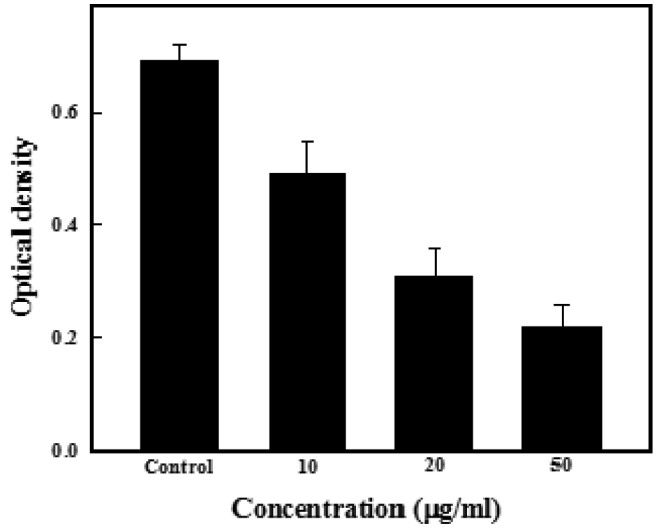

Fig. 8. *P. aeruginosa* biofilm inhibition at various concentration of the complex (0, 10, 20, 50 µg/mL) incubated for 24 h.

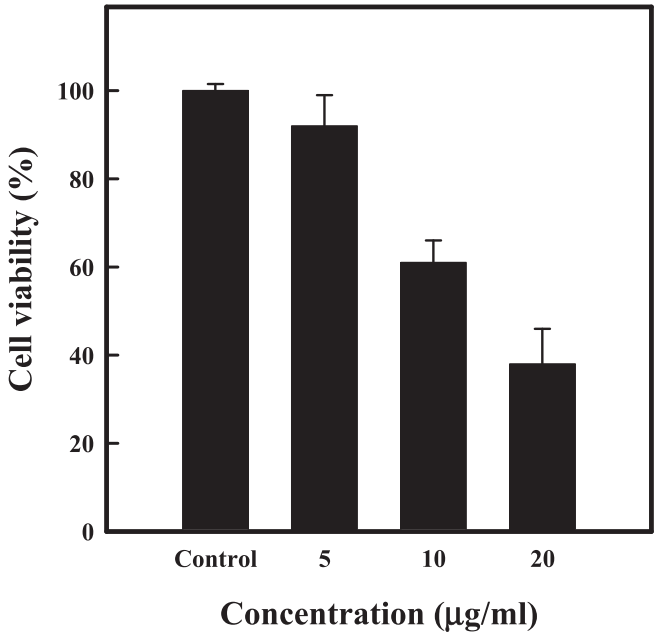

Fig. 9. MTT assay for cytotoxicity assessments in MCF-7 cells with the increasing concentration of zinc complex for 24 h. Values are mean ± SD of three independent experiments.

crystallography examination.

3.5. Biofilm inhibition by [Zn(L)Cl] complex

P. aeruginosa is a strong biofilm producer. The antimicrobial activity of zinc complex was studied by the microtiter plate assay. The data revealed the inhibition of growth pattern of *P. aeruginosa* at the increasing concentration of the complex at 20 and 50 µg/mL [Fig. 8]. The micrograph in Fig. 8 demonstrates the concentration dependent inhibition of biofilm formation by *P. aeruginosa*. The microtitre data shows 55.5 ± 5.0, and 69.3 ± 4.0% biofilm inhibition as compared to control [Fig. 8], and demonstrated that zinc complex reduced biofilm formation of P. aeruginosa. These findings corroborate with the earlier reports [32]. Zinc binds to free thiol groups, and thus, affects protein function [64]. Therefore, the quorum quenching induced by zinc complex may be an alternative for combating biofilm based microbial pathogenesis.

The MTT assay to evaluate the cytotoxicity of zinc complex in MCF-7 cell line was performed in 96 well plates. The data shown in Fig. 9 shows the reduction in MCF-7 cell line viability with increasing concentration of zinc complex after 24 h of exposure. The percent cell inhibition at 5, 10, and 20 µg/ml of zinc complex was recorded as 8%, 39%, and 62%, respectively. The LC_{50} value for zinc complex was determined, and found to be 12 µg/ml [65,66], thus suggested the cellular toxicity over MCF-7 cell line. The toxicity by the complex is generally induced by the endocytosis and release of ions, which promote Reactive oxygen species generation [32].

Protein of *Pseudomonas aeruginosa* acting as receptor [Fig. 10a] and metal complex as ligand [Fig. 10b] were docked by using PatchDock program to validate their host-guest relationships. The Dock positions of ligand was analyzed for interactions with the receptor shown in Fig. 10. The outcome exposed that the target metal complex was well buried in the active zone of the receptor [Fig. 10c]. The optimized docking output provided multiple results which were ranked according to the docking score levels. The best conformation of the docked position having the amino acids residue with the metal complex was selected on the basis of the best score result. Docking score, interface area of the interaction and three dimensional transformations for the superior docked position were found at 479.30; 3.0, −0.8, 2.3 and 14.8, 19.2, 36.9 Å, respectively. Supplementary Information Fig. S2 is showing the comparison of the docking score of position 1 with position 2 by a graphical presentation. Position 1 which fits better shows the involvement of hydrogen bond along with a preferable orientation, and Position 2 at 410.10; 0.37 −0.91 −0.58 0.68 11.77 36.24 Å is without involvement of hydrogen bond. In addition, the attractive, repulsive VdW and atomic contact energy of the best docked pose was got at −13.06, 4.31 and −10.10 kcal/mol, respectively. However, the binding energy calculated by AutoDock 4 was found to be −6.10 kcal/mol. The binding model of metal complex with receptor (1gzt.pdb) showing all the amino acid residues interacting around the metal complex is represented in Fig. 10d & f. In the binding pose, the main stabilizing factors that equilibrate the guest–host interactions are secondary forces (Fig. 10d & f) including hydrogen bonding interactions [Fig. 10d]. The metal-bound chlorine atom in the complex participates in the hydrogen bonding interaction with Leu76 at a distance of 1.92 Å. The nitrogen atom of ligand attached to metal through coordinated bond in complex acts as a hydrogen bond donor that makes a hydrogen bonding interaction from Thr2 with distance 2.02 Å. The other interactions operating between receptor and ligand were found about distance ± 3.18 Å. Based on the interaction analysis, it can be pointed out that the complex was well satisfied in the active pocket of receptor.

3.6. Luminescence properties

The luminescence behaviour of L and its zinc complex was investigated in acetonitrile at room temperature. The ligand, L exhibited a fluorescence emission bands at 318 nm and 330 nm upon excitation at 280 nm. However, the studied zinc complex showed the fluorescence emission bands at 325 nm and 338 nm under similar conditions. The increase in the fluorescence emission intensity of zinc complex may be assigned to the intraligand transitions [66,67] [Supplementary Information Fig. S3].

4. Conclusion

A new zinc complex derived from L was investigated using various

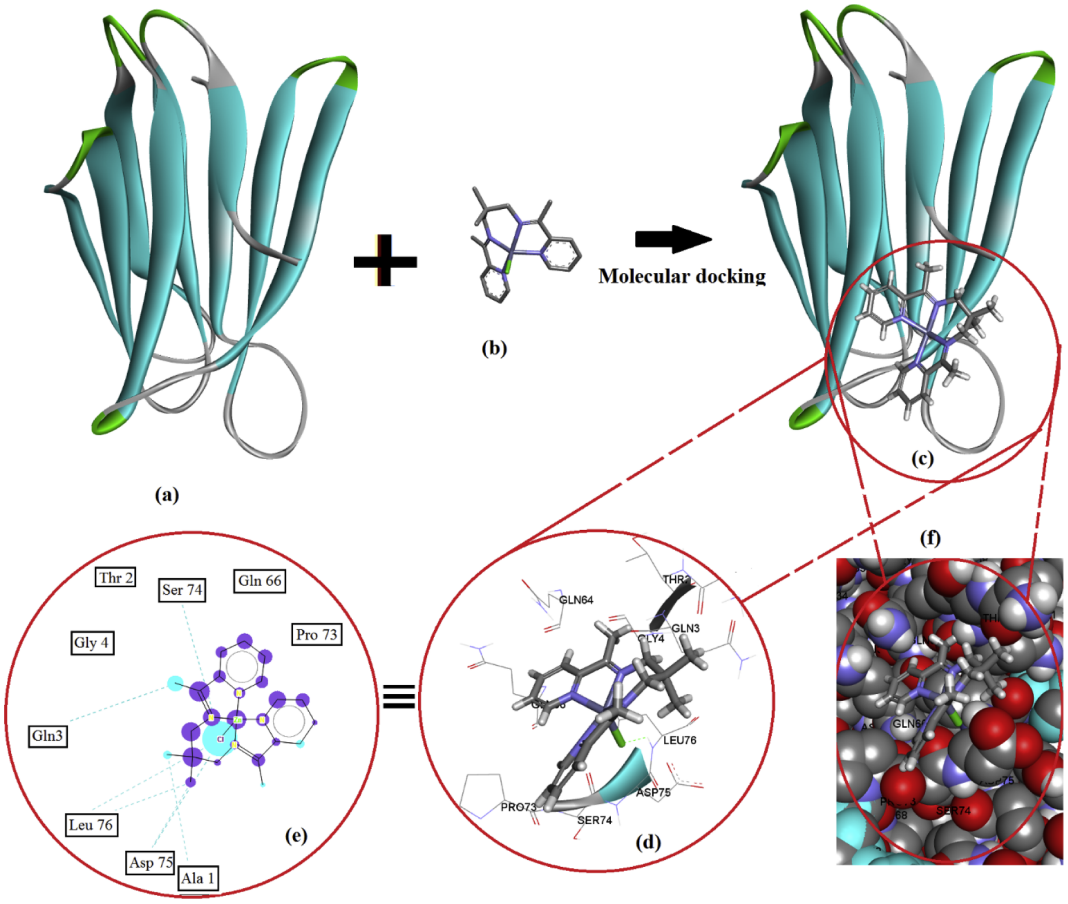

Fig. 10. Molecular docking interaction of (a) receptor, (b) metal complex, (c) docked pose showing the active site where the Zn complex cation interacts with receptor, (d) binding pose of the metal complex to the receptor showing hydrogen bond as green dashed lines, (e) ligand map showing a combined interaction pattern of hydrogen bonding, steric interactions (dotted line), and interaction overlay (a sphere centered on each atom visualizes the strength of the interactions for this specific atom) for ligand to receptor, (f) space-filling model of ligand-receptor [Supplementary Information Fig. S2].

spectroscopic studies, single crystal X-ray crystallography and DFT measurements. The complex was found pharmacologically active, and showed considerable *in vitro* antibiofilm activity against *P. aeruginosa*. Moreover, the complex was also found potential candidate against MCF-7 cancer cell line.

Acknowledgements

The authors would like to extend their sincere appreciation to the Deanship of Scientific Research at King Saud University for funding this work through research group project number RG-1436-003. R.K. and A.T.K. acknowledge for financial assistance allocated by the Ministry of Science and Higher Education to the Institute of General and Ecological Chemistry, Lodz University of Technology.

Appendix A. Supplementary data

Supplementary data to this article can be found online at https://doi.org/10.1016/j.ica.2018.12.009.

References

[1] E.M. Nolan, S.J. Lippard, Inorg. Chem. 43 (2004) 8310–8317.
[2] A. Dołęga, A. Farmas, K. Baranowska, A. Herman, Inorg. Chem. Commun. 12 (2009) 823–827.
[3] M. Azam, S.I. Al-Resayes, A.T. Kruszynska, R. Kruszynski, A. Verma, U.K. Pati, Inorg. Chem. Commun. 46 (2014) 73–80.
[4] K. Das, T.N. Mandal, S. Roy, S. Gupta, A.K. Barik, P. Mitra, A.L. Rheingold, S.K. Kar, Polyhedron 29 (2010) 2892–2899.
[5] T. Dudev, C. Lim, J. Am. Chem. Soc. 122 (2000) 11146–11153.
[6] M. Roy, A. Bauzá, A. Frontera, S. Banerjee, S. Halder, A. Saha, Polyhedron 102 (2015) 764–772.
[7] H. Torayama, T. Nishide, H. Asada, M. Fujiwara, T. Matsushita, Polyhedron 16 (1997) 3787–3794.
[8] R. Huang, A. Wallquist, D.G. Covell, Biochem. Pharmacol. 69 (2005) 1009–1039.
[9] B. Lippert, Cisplatin: Chemistry and Biochemistry of a Leading Anticancer Drug, Wiley-VCH, Zurich, 1999.
[10] D. Magda, P. Lecane, Z. Wang, Cancer Res. 68 (2008) 5318–5325.
[11] M.B. Ferrari, F. Bisceglie, G. Pelosia, P. Tarasconia, R. Albertini, S. Pinelli, J. Inorg. Biochem. 87 (2001) 137–147.
[12] I.P. Oliveri, S. Di Bella, Tetrahedron 67 (2011) 9446–9449.
[13] K. Ostrowska, K. Stadnicka, M. Gryl, B. Musielak, Ł.J. Witek, O. Bochenska, Polyhedron 133 (2017) 294–301.
[14] M. Azam, S.I. Al-Resayes, J. Mole Struct. 1107 (2016) 77–81.
[15] R. McRae, P. Bagchi, S. Sumalekshmy, Ch.J. Fahrini, Chem. Rev. 109 (2009) 4780–4827.
[16] I. Grabchev, S. Yordanova, P. Bosch, E. Vasileva-Tonkova, R. Kukeva, S. Stoyanov, R. Stoyanova, J. Mol. Struct. 1130 (2017) 974–983.
[17] H.A. Ali, S.N. Omar, M.D. Darawsheh, H. Fares, J. Coord. Chem. 69 (2016) 1110–1122.
[18] Y. Chen, X. Li Chen, Y. Chen, L. Jia, M.-H. Zeng, Inorg. Chem. Commun. 84 (2017) 182–185.
[19] M. Satterfield, J.S. Brodbelt, Inorg. Chem. 40 (2001) 5393–5400.
[20] A. Panja, Polyhedron 80 (2014) 81–89.
[21] N. Brefuel, I. Vang, S. Shova, F. Dahan, J.-P. Costes, J.-P. Tuchagues, Polyhedron 26 (2007) 1745–1757.
[22] S. Khan, A. Al Masum, M.M. Islam, M.G.B. Drew, A. Bauzá, A. Frontera, S. Chattopadhyay, Polyhedron 123 (2017) 334–343.
[23] Y.-P. Xu, Y.-H. Chen, Z.-J. Chen, J. Qin, S.-S. Qian, H.-L. Zhu, Eur. J. Inorg. Chem. (2015) 2076–2084.
[24] G.M. Sheldrick, Acta Cryst. A 71 (2015) 3–8.
[25] G.M. Sheldrick, Acta Crystallogr. A 64 (2008) 112–122.
[26] E. Prince (Ed.), International Tables for Crystallography, Volume C: Mathematical, Physical and Chemical Tables, third ed., Kluwer Academic Publishers, Dordrecht, 2004.
[27] J.R. Schmidt, W.F. Polik, WebMO Enterprise, version 0, WebMO LLC, Holland, MI,

USA, 20; http://www.webmo.net; M.J. Frisch et al., Gaussian 09, Revision D.01, Gaussian Inc, Wallingford CT, 2009.
[28] S. Grimme, J. Antony, S. Ehrlich, H. Krieg, J. Chem. Phys. 132 (2010) 154104.
[29] NIST Computational Chemistry Comparison and Benchmark Database, NIST Standard Reference Database Number 101, Release 18, October 2016, Editor: Russell D. Johnson III.
[30] R. Dennington, T. Keith, J. Millam, GaussView ver. 5, Semichem Inc., Shawnee Mission KS, 2009.
[31] M.J. Turner, J.J. McKinnon, S.K. Wolff, D.J. Grimwood, P.R. Spackman, D. Jayatilaka, M.A. Spackman, CrystalExplorer 17 (2017).
[32] S. Dwivedi, R. Wahab, F. Khan, Y.K. Mishra, J. Musarrat, A.A. Al-Khedhairy, PLoS One 9 (2014) e111289–e111297.
[33] S. Dwivedi, M.A. Siddiqui, N.N. Farshori, M. Ahamed, J. Musarrat, A.A. Al-Khedhairy, Colloids Surf. B: Biointerfaces 122 (2014) 209–215.
[34] G.M. Morris, R. Huey, W. Lindstrom, M.F. Sanner, R.K. Belew, D.S. Goodsell, A.J. Olson, AutoDock4 and AutoDockTools4: automated docking with selective receptor flexibility, J. Comput. Chem 30 (2009) 2785–2791.
[35] Molegro Virtual Docker v 5.0, Molegro ApS: Aarhus, Denmark, 2011.
[36] R. Thomsen, M.H. Christensen, MolDock, J. Med. Chem. 49 (2006) 3315–3321.
[37] D. Duhovny, R. Nussinov, H.J. Wolfson, Efficient unbound docking of rigid molecules, in: Gusfield (Ed.), Proceedings of the 2'nd Workshop on Algorithms in Bioinformatics(WABI) Rome, Italy, Lecture Notes in Computer Science 2452, Springer Verlag, 2002, pp. 185–200.
[38] D.S. Duhovny, Y. Inbar, R. Nussinov, H.J. Wolfson, Nucl. Acids. Res. 33 (2005) W363–W367.
[39] A. Gaulton, L.J. Bellis, A.P. Bento, J. Chambers, M. Davies, A. Hersey, Y. Light, S. Mcglinchey, D. Michalovich, B. Al-Lazikani, J.P. Overington, Nucl. Acids Res. 40 (2012) D1100–D1107.
[40] E. Mitchell, C. Houles, D. Sudakevitz, M. Wimmerova, C. Gautier, S. Perez, A.M. Wu, N. Gilboa-Garber, A. Imberty, Nat. Struct. Biol. 9 (2002) 918–921.
[41] C.H. Ngan, D.R. Hall, B. Zerbe, L.E. Grove, D. Kozakov, S. Vajda, Bioinformatics 28 (2012) 286–1267.
[42] N. Andrusier, R. Nussinov, H.J. Wolfson, Proteins 69 (2007) 139–159.
[43] E. Mashiach, D. Schneidman-Duhovny, N. Andrusier, R. Nussinov, H.J. Wolfson, Nucl. Acids Res. 36 (2008) W229–W232.
[44] Accelrys Software Inc., Discovery Studio Modeling Environment Releaser 4.0, Accelrys Software Inc, SanDiego, 2013.
[45] M.C. Favas, D.L. Kepert, Aspects of the stereochemistry of four-coordination and five-coordination, in: S.J. Lippard (Ed.), Progress in Inorganic Chemistry, Volume 27, John Wiley & Sons, Inc., Hoboken, NJ, USA, 1980, pp. 325–463.
[46] A.W. Addison, N.T. Rao, J. Reedijk, J. van Rijn, G.C. Verschoor, J. Chem. Soc. Dalton Trans. (1984) 1349–1356.
[47] L. Yang, D.R. Powell, R.P. Houser, Dalton Trans. (2007) 955–964.
[48] E.B. Hulley, V.A. Williams, W.D. Morris, P.T. Wolczanski, K. Hernandez-Burgos, E.B. Lobkovsky, T.R. Cundari, Polyhedron 84 (2014) 182–191.
[49] V.A. Williams, E.B. Hulley, P.T. Wolczanski, K.M. Lancaster, E.B. Lobkovsky, Chem. Sci. 4 (2013) 3636–3648.
[50] S. Khan, A. Al Masum, M.M. Islam, M.G.B. Drew, A. Bauza, A. Frontera, S. Chattopadhyay, Polyhedron 123 (2017) 334–343.
[51] R. Kruszynski, Inorg. Chim. Acta 371 (2011) 111–123.
[52] R. Kruszynski, Struct. Chem. 21 (2010) 87–97.
[53] R. Kruszynski, T. Sieranski, M. Swiatkowski, M. Zielak, J. Wojciechowski, M. Dzierzawsk, B. Lewinski, J. Coord. Chem. 67 (2014) 1332–1352.
[54] M. Swiatkowski, R. Kruszynski, Acta Crystallogr. C 73 (2017) 1144–1150.
[55] R. Kruszynski, M. Swiatkowski, J. Saudi Chem. Soc. (2018), https://doi.org/10.1016/j.jscs.2018.01.003.
[56] C.R. Groom, I.J. Bruno, M.P. Lightfoot, S.C. Ward, Acta Crystallogr. B 72 (2016) 171–179.
[57] M. Swiatkowski, R. Kruszynski, J. Coord. Chem. 70 (2017) 642–675.
[58] R. Sarkar, A. Hens, K.K. Rajak, Synthesis, characterization and DFT study of oxorhenium(V) complexes incorporating quinoline based tridentate ligands, RSC Adv. 5 (2015) 15084–15095.
[59] J. Bernstein, R.E. Davis, L. Shimoni, N.-L. Chang, Angew. Chem. Int. Ed. Engl. 34 (1995) 1555–1573.
[60] G.R. Desiraju, T. Steiner, The Weak Hydrogen Bond in Structural Chemistry and Biology, Oxford University Press, Oxford, 1999.
[61] R. Kruszynski, T. Sieranski, Cryst. Growth Des. 16 (2016) 587–595.
[62] M. Shakir, M. Azam, Y. Azim, S. Parveen, A.U. Khan, Polyhedron 26 (2007) 5513–5518.
[63] K. Nakamoto, Infrared and Raman Spectra of Inorganic and Coordination Compounds, fourth ed., Wiley Interscience, New York, 1986.
[64] C.A. Blindauer, M.D. Harrison, J.A. Parkinson, A.K. Robinson, J.S. Cavet, N.J. Robinson, P.J. Sadler, Proc. Natl. Acad. Sci. U.S.A. 98 (2001) 9593–9598.
[65] S. Dwivedi, Q. Saquib, A.A. Al-Khedhairy, J. Ahmad, M.A. Siddiqui, J. Musarrat, Colloids Surf. B: Biointerfaces 132 (2015) 290–298.
[66] R. Wahab, N.K. Kaushik, N. Kaushik, E.H. Choi, A. Umar, S. Dwivedi, J. Musarrat, A.A. Al-Khedhairy, J. Biomed. Nanotechnol. 9 (2013) 1181–1189.
[67] Y.-W. Dong, R.-Q. Fan, W. Chen, H.-J. Zhang, Y. Song, X. Du, P. Wang, L.-G. Wei, Y.-L. Yang, RSC Adv. 6 (2016) 110422–110432.